Kauppinen, Minttu M.; Słapa, Ewa N.; González Escobedo, José Luis; Puurunen, Riikka L.; Honkala, Karoliina

Computational insight into the selectivity of γ-valerolactone hydrodeoxygenation over Rh(111) and Ru(0001)

Published in:
Surface Science

DOI:
10.1016/j.susc.2024.122624

Published: 01/01/2025

Document Version
Publisher's PDF, also known as Version of record

Surface Science 751 (2025) 122624

Contents lists available at ScienceDirect

Surface Science

journal homepage: www.elsevier.com/locate/susc

Computational insight into the selectivity of γ-valerolactone hydrodeoxygenation over Rh(111) and Ru(0001)

Minttu M. Kauppinen [a], Ewa N. Słapa [a], José Luis González Escobedo [b], Riikka L. Puurunen [b], Karoliina Honkala [a,*]

[a] Department of Chemistry, University of Jyväskylä, Nanoscience Center, P.O. Box 35 (YN), FI-40014, Finland
[b] Department of Chemical and Metallurgical Engineering, School of Chemical Engineering, Aalto University, P.O. Box 16100, 00076, AALTO, Finland

ARTICLE INFO

Keywords:
Biomass
Density-functional theory
Hydrodeoxygenation
Hydrocarbons
Microkinetic analysis
γ-valerolactone
Selectivity
Coverage

ABSTRACT

The observed difference in the selectivity towards alkane, ketone, and alcohol hydrodeoxygenation products over Ru and Rh catalysts is explored using a combination of density functional theory and microkinetics. Using γ-valerolactone as a model compound, we investigate the reaction mechanism in order to identify selectivity determining species. The effect of the coadsorbed water molecule as well as the higher adsorbate surface coverage on reaction barriers and energies is explored as well. The performed calculations suggest that the desired alkane product is formed from a ketone intermediate on Ru, and through both ketone and alcohol on Rh, although the selectivity towards alkane on Rh is much lower than on Ru.

1. Introduction

Lignocellulosic biomass is the most abundant renewable carbon source on Earth, and is considered as a genuine alternative to fossil feedstocks in the production of fuels and chemicals [1]. A multitude of compounds can be formed from biomass, which can be used further as platform molecules in biorefineries [2]. Among the molecules derived from lignocellulosic biomass, levulinic acid (LA) has been identified as a key platform chemical [3], because it is a precursor to a wide set of chemicals and includes a number of large market volume species such as methyltetrahydrofuran, levulinate esters, acrylic acid, and γ-valerolactone (GVL). However, LA contains only five carbon atoms, so its direct conversion to hydrocarbons used for liquid fuel production is not feasible. One viable approach to increase the carbon chain length is aldol condensation, a coupling reaction in which carbon–carbon bonds are formed [4–8]. The synthesized C_{10} dimers are slightly branched and contain carboxyl, carbonyl, and lactone groups [5], but they are unstable and corrosive, making LA dimers unsuitable to use directly as fuels.

Further valorization of LA dimers by removing oxygen moieties via hydrodeoxygenation (HDO) can lead to valuable products such as biofuels [9,10]. Recently, the HDO process was explored by some of us for the conversion of a simplified representative of a LA dimer, γ-nonalactone (GNL) to various hydrocarbon species [11]. ZrO_2 supported Ru, and to lesser extent Rh, were found to be selective towards the desired saturated hydrocarbons, which constitute the basis of biofuel. In addition, the Ru and Rh catalysts also promoted the formation of mostly C_8 alcohols and ketones [11]. Another common approach to obtain fuel components from LA is its conversion to GVL, which has favourable physico-chemical properties such as stability in water and in the presence of air [12]. GVL can be processed catalytically to a numerous valuable species such as 2-methyltetrahydrofuran (MTHF) [13,14], butene oligomers [15], or 5-nonanone [16].

GVL and GNL species, shown in Fig. 1, differ only by the substituent at the C4 carbon, which is a pentyl group for GNL and methyl group for GVL. In previous DFT calculations, GVL conversion to MTHF and alcohols (butan-2-ol, pentan-2-ol), 2, 4-propanediol (PDO) was considered on Ru(0001) [17,18]. Alcohol production was proposed to proceed from GVL via surface ring-opening giving to an adsorbed acyl intermediate followed by decarbonylation [17]. The activation energy for acyl hydrogenation was calculated to be as high as 1.7 eV for 2-pentanol formation making this step rate-controlling [18]. GVL adsorption was proposed to compete with its HDO product adsorption due to nearly equal adsorption energies of these species [18]. However, the formation of products such as ketones and hydrocarbons, essential for biofuel components was not considered. Additionally, ketone and hydrocarbon formation might require higher temperatures [11] than the ones available in the experimental data on which these DFT studies were based.

* Corresponding author.
E-mail address: karoliina.honkala@jyu.fi (K. Honkala).

https://doi.org/10.1016/j.susc.2024.122624
Received 28 June 2024; Received in revised form 6 October 2024; Accepted 7 October 2024
Available online 16 October 2024

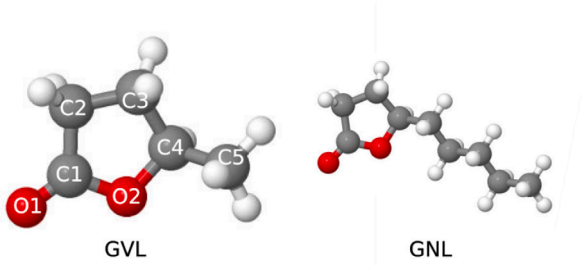

Fig. 1. γ-Valerolactone showing the atom numbering used in this work (left) and γ-nonalactone (right).

In the present work, we performed a computational multiscale study to elucidate the reaction mechanism of GVL conversion towards alcohol, ketone, and alkane, and to understand factors controlling selectivity on Ru(0001) and Rh(111) surfaces. We employ GVL as a model compound for GNL, with GVL-derived butane acting as representative for the longer-chain alkanes obtained from GNL. The first-principles microkinetic analysis is employed to unravel the reaction selectivity under operating catalyst conditions. The effect of higher coverage and coadsorbed water was investigated for selectivity controlling steps. We compare our results to the previously reported experimental data on solvent-free GNL hydrodeoxygenation [11]. Our results suggest that both Ru and Rh metal surfaces are most selective towards alcohol. Ru is found to be more selective towards alkane than Rh. On Ru, the alkane product is produced solely through the ketone intermediate, whereas on Rh, both the alcohol and ketone species contribute to alkane production. The selectivity is an interplay between the hydrogenation/dehydrogenation barriers of the shared surface intermediate, and the favoured desorption from the surface.

2. Methods

2.1. Computational details

The DFT calculations were carried out in the grid-based projector augmented wave (PAW) formalism using the GPAW software [19–22]. The BEEF-vdW [23] density functional was chosen in order to include dispersion forces. PAW [24] setups were employed to represent the core electrons of Ru and Rh in the frozen-core approximation.

The Rh(111) and Ru(0001) surfaces were modelled with four-layers thick 3×3 (and 2×2 for Ru) surface cells and the two bottom layers were fixed at optimized bulk positions. The slabs were periodic in the plane parallel to the surface and nonperiodic in the perpendicular direction. At least 5 Åof vacuum was added to each side of the slab in the perpendicular direction. A Monkhorst–Pack mesh of $(4 \times 4 \times 1)$ and $(6 \times 6 \times 1)$ k-points were used for sampling the reciprocal space for the 3×3 and 2×2 sized surface slabs, respectively. Gas-phase species were evaluated at the Γ-point in a non-periodic computational cell with a side length of 18 Å. A grid basis with a 0.19 $Å^{-1}$ maximum grid spacing was used in all the calculations, and structures were allowed to relax until the maximum residual force was below 0.05 eV $Å^{-1}$. Transition states were located using a climbing image automated nudged elastic band (CI-AutoNEB) method [25–28], and were verified by the presence of a single imaginary vibrational mode along the reaction coordinate.

For each of the reaction intermediates several minimum structures were localized using geometry optimization calculations. Similarly for localization of TSs a few nudged elastic band (NEB) [25–28] calculations were performed and often more than one converged to a saddle point along the reaction coordinate corresponding to an activation barrier for each elementary step. The structures of the optimized species with the lowest energies are openly available to download from the Finnish Fairdata service at https://doi.org/10.23729/ea2e013c-52ac-49d3-9c70-106b49e98920.

Vibrational modes were determined for the lowest energy minima and TS structures. Subsequently, the vibrational analysis was conducted for all gas and adsorbed species (at the harmonic limit and excluding atoms of the metal slab) in order to calculate the zero-point energies (ZPE).

The forward (backward) activation energy for each elementary step was calculated as a difference of the energy of the localized TS and the energy of the reactants (products).

$$E_a = E_{TS} - E_i \tag{1}$$

Adsorption/desorption energies of reactants and products were computed with respect to their gas phase counterparts and the pure surface slab. Since the reaction mechanism involves many (de-)hydrogenation steps, the activation and adsorption/desorption energies include both the electronic activation energy and the ZPE correction.

Microkinetic modelling was performed using our own Python code. The system of differential equations was solved by numerical integration employing the solve_ivp function as implemented in the Scipy package [29] scipy.integrate.

Rate constants for activated surface reactions were calculated using transition state theory in the harmonic approximation:

$$k_{surf} = \frac{k_B T}{h} \exp\left[-\frac{E_a}{k_B T}\right] \tag{2}$$

where E_a is the ZPE corrected activation energy, k_B is the Boltzmann constant, T is the temperature, h is Planck's constant.

Adsorption rate constants were calculated as:

$$k_{ads} = P \frac{A}{\sqrt{2\pi m k_B T}}, \tag{3}$$

where P is the partial pressure, m is the mass of a single molecule, and A is the adsorption area, approximated as 1×10^{-19} m^2.

Desorption rate constants were calculated from the adsorption rate constant via the equilibrium constant

$$k_{des} = k_{ads} exp\left[\frac{-\Delta G^\circ}{k_B T}\right], \tag{4}$$

where ΔG° is the standard Gibbs free energy change of adsorption. The Gibbs free energies of the gas-phase species were calculated using the IdealGasThermo class as implemented in ASE [21,22]. The Gibbs free energy of the surface species was approximated within the harmonic limit using the HarmonicThermo class found in ASE [21,22]. The simulations were performed under steady reaction conditions with pressures set to 1 bar for hydrogen, and zero for all other species. The models were solved for reaction temperatures from 513 to 593 K in 20 K intervals. The chosen conditions correspond to initial zero conversion conditions, and the temperature range is centred at the investigated temperature in our experimental work [11]. The selectivity towards each product is defined as the ratio between the production rate of that product and the sum of production rates of all three products.

3. Results & discussion

The products of GVL conversion analysed in this work are butan-2-one (butanone), butan-2-ol (butanol) and butane. Previous DFT calculations [17,18] suggest that the reaction towards these three decarbonylation products follows the reaction mechanism presented in Fig. 2. The reaction starts with the GVL adsorption on the metal surface followed by three elementary steps: ring opening, decarbonylation, and terminal carbon hydrogenation. These elementary steps are common for all three products and thus should have no control on the product selectivity. The final intermediate before the reaction pathway diverges is a transient species **IV** [$C_4H_9O^*$], referred herein as a "key intermediate". Subsequently, the reaction towards the desired alkane may proceed through an alcohol (blue arrows) or a ketone (red arrows) intermediate (Fig. 2).

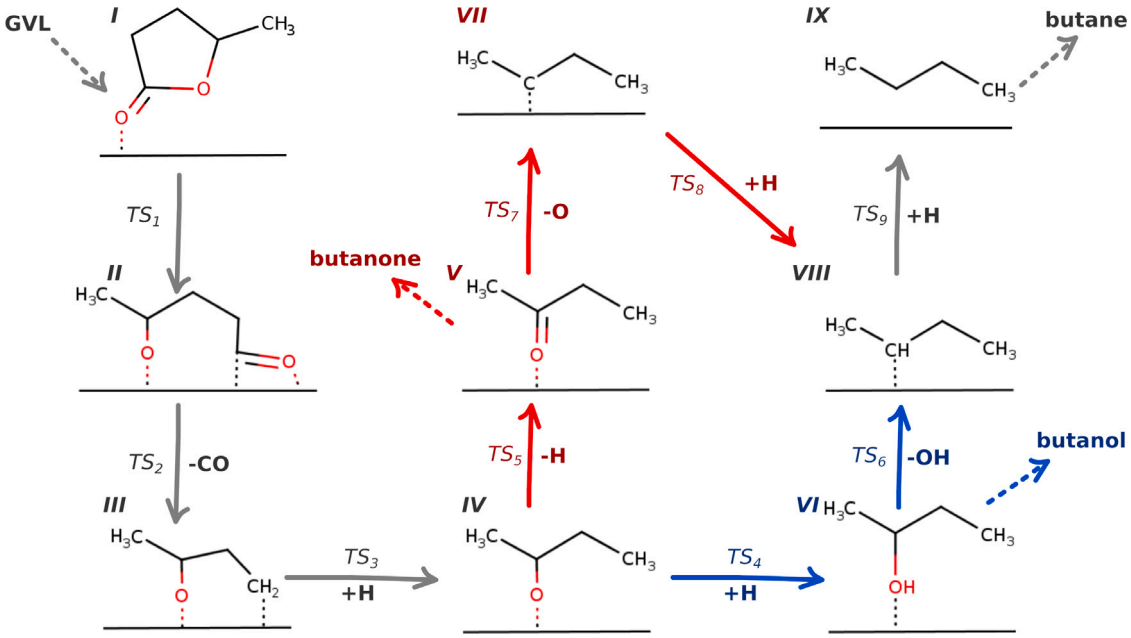

Fig. 2. A reaction network for GVL catalytic transformation. Dotted arrows represent adsorption/desorption processes. Red and blue arrows indicate pathways leading to alkane production through ketone and alcohol intermediates respectively.

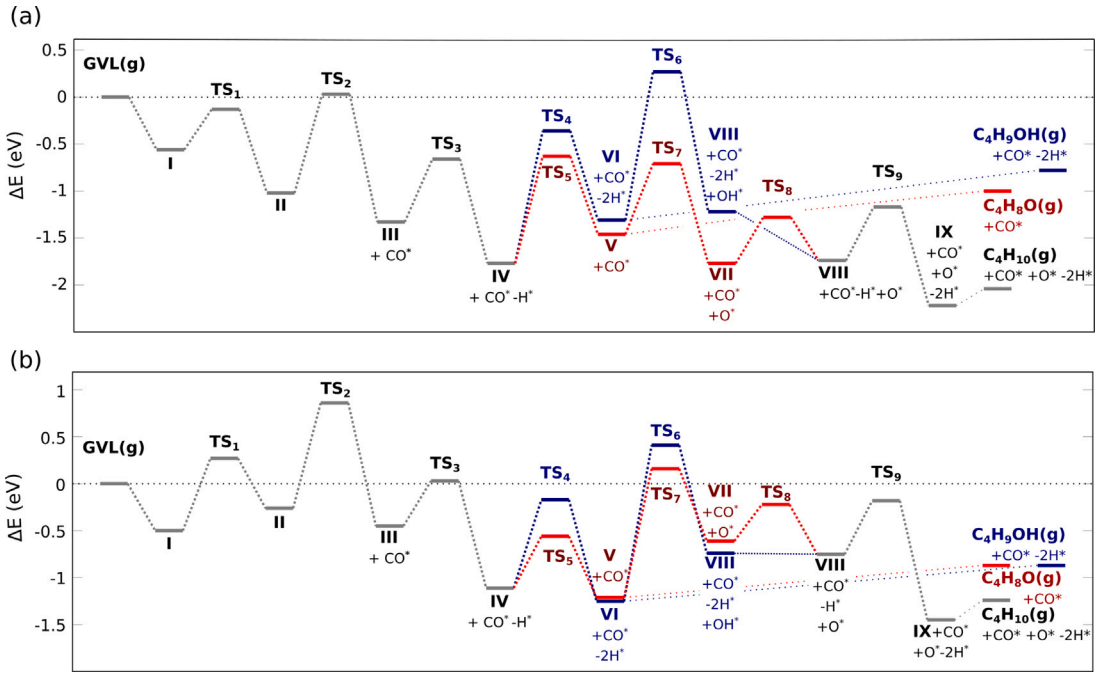

Fig. 3. The potential energy surface of GVL conversion over Ru (top) and Rh (bottom) surfaces. Atomic hydrogen, oxygen as well as carbonyl and hydroxyl groups are adsorbed on a separate slab, so in order to keep the same number of atoms an energy of a metallic slab is correspondingly added or subtracted to/from intermediate species.

3.1. HDO mechanism over Ru(0001) and Rh(111)

We have considered the reaction network, given in Fig. 2, for GVL conversion to three studied decarbonylation products on Ru(0001) and Rh(111) surfaces. Fig. 3 summarizes the reaction energy landscape and the calculated reaction and activation energies are collected into Table 1. The most stable adsorption geometries for the reactant and the three product species on the Ru(0001) and Rh(111) are given Fig. 4.

3.1.1. Adsorption of reactant and product species

The most stable conformation of GVL on both Ru and Rh surfaces was found to bind through the substituent oxygen O1 (Fig. 1) with adsorption energies of ca. −0.5 eV. This value is less exothermic than the values of −1.46 eV [17], −0.72 eV [30] and -1 eV [18] calculated previously employing the PBE functional with the DFT-D3 correction on Ru(0001). Also in these previous studies GVL adsorbed via not only carbonyl oxygen (O1) but also carbonyl carbon (C1) [30] and ring oxygen (O2) [17,18]. The difference can be due to the functional used. However, our calculations showed that the adsorbed GVL corresponding to the aforementioned geometries were higher in energy by 0.25 to 0.4 eV compared to the lowest in energy conformation.

The adsorption geometries of the decarbonylation products are very similar on both metal surfaces. Butanol interacts with the metal atom through the oxygen of the hydroxyl group and its adsorption energies are −0.53 eV on Ru and −0.38 eV on Rh. Again, our adsorption energy on Ru is less exothermic than the previously reported value of ∼ −1

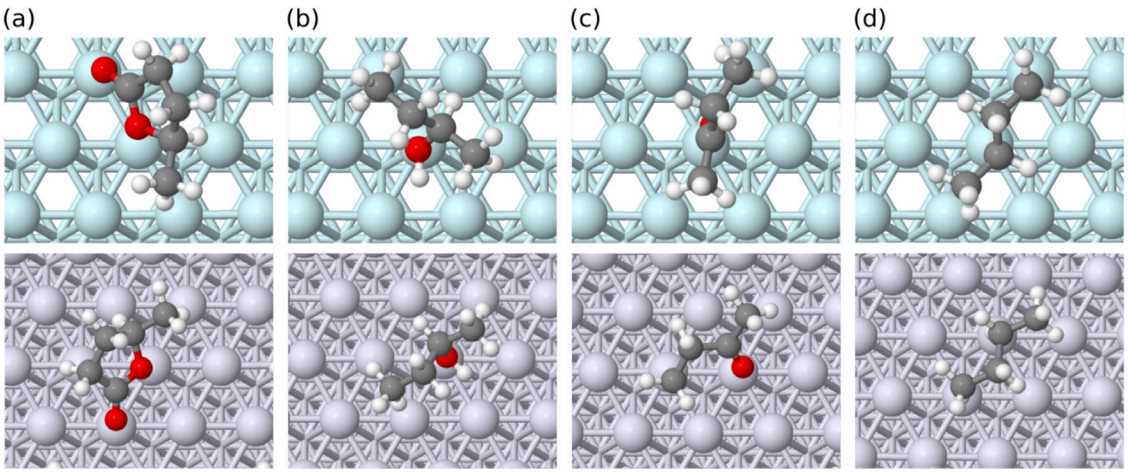

Fig. 4. Top down view of the optimized structures of adsorbed reaction substrate and relevant products: (a) GVL, (b) butanol, (c) butanone, (d) butane on the 3 × 3 surface cells of Ru(0001)(top) and Rh(111) (bottom) surfaces.

Table 1
Reaction energies (ΔE) and activation energies (E_a) in eV for each elementary step of the GVL conversion over Ru(0001) and Rh(111) surfaces. * refers to an empty site.

Process	Reaction	TS	Ru(0001)		Rh(111)	
			ΔE	E_a	ΔE	E_a
GVL adsorption	**GVL** +* ⇌ **I**	–	−0.56	–	−0.50	–
Ring opening	**I** ⇌ **II**	1	−0.45	0.43	0.24	0.76
Decarbonylation	**II** +* ⇌ **III** +CO*	2	−0.32	1.04	−0.19	1.13
Hydrogenation	**III** +H* ⇌ **IV** +*	3	−0.43	0.68	−0.66	0.48
Hydrogenation	**IV** +H* ⇌ **VI** +*	4	0.46	1.41	−0.14	0.93
Dehydrogenation	**IV** +* ⇌ **V** +H*	5	0.31	1.13	−0.10	0.54
Dehydroxylation	**VI** +* ⇌ **VIII** +OH*	6	0.09	1.58	0.52	1.66
Deoxygenation	**V** +* ⇌ **VII** +O*	7	−0.31	0.75	0.59	1.37
Hydrogenation	**VII** +H* ⇌ **VIII** +*	8	0.03	0.49	−0.13	0.40
Hydrogenation	**VIII** +H* ⇌ **IX** +*	9	−0.49	0.57	−0.70	0.56
Butanol desorption	**VI** ⇌ **butanol** +*	–	0.53	–	0.38	–
Butanone desorption	**V** ⇌ **butanone** +*	–	0.46	–	0.34	–
Butane desorption	**IX** ⇌ **butane** +*	–	0.19	–	0.21	–

eV [18]. Butanone adsorbs on the surface through the carbonyl group oxygen with adsorption energy of −0.46 eV on Ru and −0.34 eV on Rh. The obtained adsorption geometries as well as adsorption energies of alcohol and ketone agree well with the DFT results of isopropanol and acetone adsorption on Rh(111) and Ru(0001) [31]. Finally, butane adsorption on both metals is the weakest, with an adsorption energy of ∼ −0.2 eV.

3.1.2. Ring opening

Regarding the overall reaction mechanism, the first step is always GVL ring opening. Previous studies show that the ring opening preferably proceeds via C1-O1 bond breaking on the Ru(0001) surface forming an acyl species **II** [$CH_3OC_2H_4CO^*$] [17,18]. In our calculations the cleavage of C–O bond is exothermic by −0.45 eV on Ru(0001) whereas on Rh(111) the ring opening is slightly endothermic by 0.24 eV. The acyl species **II** migrates, so that the O2 atom resides in a hollow site (fcc on Ru and hcp on Rh) while the terminal CO group is placed horizontally on the bridge site (Figure Ssth). The corresponding activation energies for this step are 0.43 eV and 0.76 eV on Ru and Rh, respectively.

3.1.3. Decarbonylation and hydrogenation

Subsequent decarbonylation of acyl species **II** leads to a C_4 species **III** and an abstracted CO. CO adsorbs very strongly on both Ru(0001) and Rh(111), and could lead to the poisoning of the surface. Instead, CO can likely be converted to methane by reacting with hydrogen as both metals are efficient methanation catalysts [32–34]. No self poisoning effect was observed in our previous experimental work, and methane was observed as a product, which supports the interpretation that CO is removed as methane. The consideration of the entire CO methanation reaction network with DFT is out of the scope of the current paper. Decarbonylation is mildly exothermic on both surfaces and the cleavage of the C–C bond has a ∼ 1 eV barrier. The forming intermediate **III** [$CH_2CH_2COCH_3$] binds to the surface via the terminal methyl group on a top site and via the oxygen on a hollow site. In the last common reaction step for all products, **III** is hydrogenated. Our calculations show that methyl group hydrogenation and key reaction intermediate (**IV** [$CH_3CH_2COCH_3$]) formation is exothermic and with a XX eV barrier, making it more favourable than hydrogenation of the ketonic oxygen which is endothermic and has a much higher barrier (by 0.6 eV).

3.1.4. Butanol formation

From the key intermediate **IV** the reaction pathway can follow one of the two parallel routes. Both routes can lead to butane production via either a butanol or butanone intermediate. However, these intermediates may also desorb from the surface before being converted to alkane.

The computed activation barrier for hydrogenation of key intermediate to butanol (**VI**) is 0.93 eV for Rh(111) and 1.41 eV for Ru(0001). A similarly high barrier was found previously for isopropanol formation on Ru(0001) [31]. Once formed, the adsorbed butanol can undergo dehydroxylation to species **VIII** [$C_4H_9^*$], which is the final intermediate before the formation of the butane product. Here we emphasize that the calculated butanol desorption energy is much lower than the high activation barrier of dehydroxylation that was found to be 1.58 eV on Ru and 1.66 eV on Rh, which are the highest barriers located for the studied GVL transformation reaction network. Furthermore, the butanol

formation reaction is endothermic on Ru, making this pathway to butane formation altogether unfavourable. However, increasing hydrogen pressure in experiments might make alcohol formation more plausible by shifting the balance towards hydrogen consuming reactions.

3.1.5. Butanone formation

Alternatively, the key intermediate can undergo dehydrogenation to butanone. We find that activation energy of butanone formation is about 0.4 eV lower than that of butanol formation on both metal surfaces. On Ru(0001), the reaction is also less endothermic than the competing hydrogenation to alcohol. On Rh(111) both reactions are slightly exothermic. The formed butanone interacts with the metal surfaces through its oxygen atom having desorption energies of 0.46 eV and 0.34 eV on Ru and Rh surfaces, respectively. Similar to butanol, desorption into gas-phase is more favourable than the subsequent deoxygenation reaction. Butanone deoxygenation via $\mathbf{TS_7}$ has a barrier of 0.75 eV on Ru and 1.37 eV on Rh. The reaction gives intermediate **VII** [$C_4H_8^*$] and the reaction is exothermic on Ru and endothermic on Rh.

3.1.6. Butane production

The deoxygenated species **VII** may undergo two consecutive hydrogenation steps to form butane. First, one proceeds via $\mathbf{TS_8}$ giving intermediate **VIII**. Although the product **VIII** is the same as the butanol dehydroxylation step, the hydrogenation reaction has much lower barriers of only 0.49 and 0.40 eV on Ru and Rh, respectively. The second hydrogenation step forms the adsorbed butane, **IX** [C_4H_1O], and the reaction is exothermic on both surfaces with forward activation barrier of 0.57 and 0.56 eV on Ru and Rh, respectively. Finally, butane may be released in to the gas phase with a desorption energy of 0.2 eV.

3.1.7. DFT discussion

So far our DFT results seem to suggest that the Ru catalyst should be more active towards hydrocarbon production compared to Rh, due to more favourable thermodynamics and much lower decarbonylation and deoxygenation barriers. This result is in accordance with our previous experiments on GNL conversion [11] (see SI for previously unpublished data on the reaction system of the cited study).

The experimental data suggests that the formation of C_8 products and methane might have proceeded through the decarbonylation of GNL followed by the methanation of the resulting CO [11]. Furthermore, alcohols might be important intermediates in the formation of hydrocarbons, whereas the role of ketones in the reaction mechanism was not clear [11]. However, the barriers for dehydrogenation of the key intermediate **IV** to ketone and subsequent deoxygenation are much lower than hydrogenation to alcohol and following dehydroxylation on both studied surfaces. This suggests that alkane production is more likely to proceed not through alcohol, but through a ketone intermediate.

In order to further investigate the selectivity towards possible products, we employ first principles microkinetic modelling [35–39]. Microkinetic analysis is vital for understanding how the competing reaction pathways proceed under experimentally relevant reaction conditions, which is not always readily apparent from DFT derived reaction energy landscapes alone.

3.2. Microkinetic analysis

In addition to the reaction steps discussed in the previous sections, we have included some additional steps in order to have a closed reaction pathway suitable for microkinetic analysis: (1) a reaction pathway for water formation from the adsorbed oxygen atom formed during ketone deoxygenation (2) a composite step that feeds key intermediate to the surface. While it is possible that any elementary step in the reaction network could, in principle, either control or inhibit the overall rate, here we are mainly interested in the selectivity control towards butanone, butanol, and butane. The selectivity should not depend sensitively on the rates of the preceding reaction steps such as GVL ring opening and decarbonylation, as those are common to all pathways leading to the three products. The rate of the feeding step was set to a value of 0.001 s^{-1}, as this resulted in the best numerical stability of the solver. Several other rates were tested over four orders of magnitude to verify that the rate does not affect the selectivity of the reaction pathways. It was found that regardless of the feeding rate, the sum of the rates of production of butanol, butane, and butanone is always equal to the feed rate. The elementary steps included in the microkinetic model are presented in Table 2.

Table 2
Elementary steps included in the microkinetic model. Note that for all steps both the forward and reverse reactions are included in the model.

R1	$H_{2(g)} + 2^* \underset{k_{r1}}{\overset{k_{f1}}{\rightleftharpoons}} H^* + H^*$
R2	$butanol^* \underset{k_{r2}}{\overset{k_{f2}}{\rightleftharpoons}} butanol_{(g)} + *$
R3	$butanone^* \underset{k_{r3}}{\overset{k_{f3}}{\rightleftharpoons}} butanone_{(g)} + *$
R4	$key\ intermediate^* + H^* \underset{k_{r4}}{\overset{k_{f4}}{\rightleftharpoons}} butanol^* + *$
R5	$key\ intermediate^* + * \underset{k_{r5}}{\overset{k_{f5}}{\rightleftharpoons}} butanone^* + H^*$
R6	$butanol^* + * \underset{k_{r6}}{\overset{k_{f6}}{\rightleftharpoons}} dehydroxed^* + OH^*$
R7	$butanone^* + * \underset{k_{r7}}{\overset{k_{f7}}{\rightleftharpoons}} deoxed^* + O^*$
R8	$deoxed^* + H^* \underset{k_{r8}}{\overset{k_{f8}}{\rightleftharpoons}} dehydroxed^* + *$
R9	$dehydroxed^* + H^* \underset{k_{r9}}{\overset{k_{f9}}{\rightleftharpoons}} butane^* + *$
R10	$butane^* \underset{k_{r10}}{\overset{k_{f10}}{\rightleftharpoons}} butane_{(g)} + *$
R11	$OH^* + H^* \underset{k_{r11}}{\overset{k_{f11}}{\rightleftharpoons}} H_2O^* + *$
R12	$OH^* + OH^* \underset{k_{r12}}{\overset{k_{f12}}{\rightleftharpoons}} H_2O^* + O^*$
R13	$O^* + H^* \underset{k_{r13}}{\overset{k_{f13}}{\rightleftharpoons}} OH^* + *$
R14	$H_2O^* \underset{k_{r13}}{\overset{k_{f13}}{\rightleftharpoons}} H_2O_{(g)} + *$

3.2.1. Favoured reaction pathway and product selectivity

The selectivities towards butanol, butane, and butanone on Ru(0001) and Rh(111) are summarized as a function of temperature in Fig. 5. On both surfaces, the reaction is mostly selective towards butanol production at all simulation temperatures. This is probably due to the high hydrogen coverage (>0.9 ML) observed in all of the simulations, which heavily favours the hydrogenation of the key intermediate over the dehydrogenation reaction. In addition, butanol desorption is much faster compared to the butane formation steps from either the butanol or butanone intermediates. On Rh(111) the selectivity towards butanol decreases slightly with temperature. This can be rationalized as the butanol and butanone production steps have similar energetics on Rh(111), but the butanol production step has a higher barrier which makes it more sensitive to temperature. As temperature increases, butane production becomes more feasible on both surfaces. On Rh(111) the change is too small to be seen in Fig. 5, but on Ru(0001) the butane selectivity increases from 1% to 40% across the tested temperature range. The butanone selectivity does not vary with temperature on Ru(0001).

Inspection of the individual elementary step rates reveals that the reaction proceeds towards butane through different pathways on the two surfaces. On Ru(0001) butane is produced only via the butanone deoxygenation step, while the butanol dehydroxylation step has a negligible contribution to the overall butane production rate. In contrast, on Rh(111), though the overall rate is very small, both the butanol and butanone pathways are active. At 553 K the butanol pathway contributes 70% to the overall butane production rate.

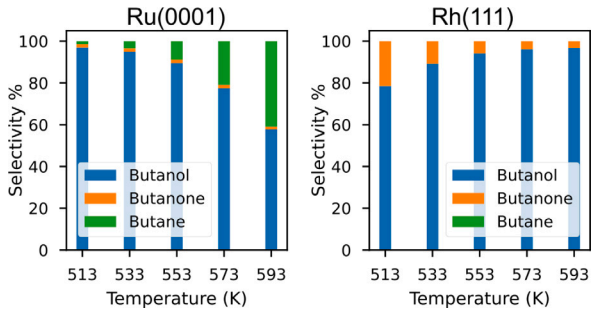

Fig. 5. Selectivities towards the butanol, butanone, and butane products on ruthenium (left) and rhodium (right) surface at different temperatures.

3.3. Modifications to the MKM

As discussed above, the butanol conversion to butane has a very low rate on Ru(0001) contributing almost nothing to the overall butane production, while on Rh(111) the conversion of butanol intermediate to butane is overshadowed by the desorption of butanol. Although butanol production from GVL is observed in various experiments, [14,17], our previous results suggest that alcohols are also important intermediates in the overall HDO process, not merely final products [11]. The reaction may be very sensitive to even small changes in the reaction energy profile, which ultimately depend on the choice of the computational catalyst model. Therefore, in order to find out whether the conversion to butane through butanol may be rationalized, we have performed further calculations on modified computational catalyst models.

3.3.1. The effect of coadsorbed water

In the perfectly stoichiometric idealized HDO reaction the oxygen is removed from the biomass as water. As discussed in our previous experimental studies of GNL conversion,[11] water is indeed produced in significant quantities during the catalytic process. Moreover, it has been demonstrated both experimentally and theoretically, that water enhances the reactivity of Ru and Rh for acetone hydrogenation [31]. Explicitly including a coadsorbed water molecule was observed to significantly lower acetone hydrogenation barriers, explaining the role of the water solvent in LA conversion to GVL [31]. Therefore we have explored the effect of coadsorbed water on the energetics of a few important surface intermeditates and transition states along the GVL hydrodeoxygenation reaction pathway.

In order to explore the interaction of coadsorbed water with other adsorbates, a H_2O molecule was placed on the metal surface in the vicinity of the adsorbate/transition state of interest. Subsequently, a geometry optimization calculations were performed for the new structures. The most stable structures of the key intermediate **IV** with and without coadsorbed H_2O on Rh and Ru are presented in Fig. 6. The presence of water modifies the geometry of the key intermediate species. The key intermediate is displaced from the fcc hollow site, and moves to the top/bride site on Ru/Rh. Furthermore, a hydrogen bond is formed between the oxygen atom of **IV** and one of the hydrogens from the water molecule. The bond length is 1.52 Å on Ru, and 2.16 Å on Rh. The difference between the energy of the co-adsorbed key intermediate and water on Ru compared to the infinitely separated case is negligible, whereas for Rh the infinitely separated configuration is 0.16 eV more stable. The interaction between the key intermediate and the water molecule can be described as slightly repulsive, and is in line with the elongated intermolecular O–H bond.

As a consequence of the interaction with water, the energetics of the key intermediate hydrogenation and dehydrogenation reactions are modified as well (see Fig. 7). On Ru(0001), the hydrogenation activation barrier decreases by 0.4 eV compared to the non-coadsorbed case. The same stabilization effect is observed also for the dehydrogenation

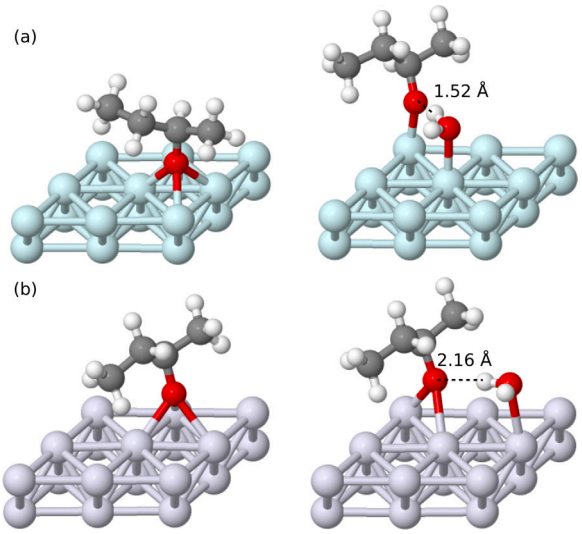

Fig. 6. Optimized structure of a key species **IV** adsorbed on a 3 × 3 supercell on (a) ruthenium and (b) rhodium; on the right the structures with coadsorbed water molecule. The periodic images of the computational cells are left out of the figure for clarity.

reaction of the key intermediate, with the activation barrier decreasing by 0.4 eV. On Rh(111), the hydrogenation barrier for the co-adsorbed system is increased by 0.2 eV compared to the infinitely separated system. This is due to the fact that the transition state is slightly more destabilized by the presence of the water than the key intermediate. In contrast, the transition state for the dehydrogenation reaction is not destabilized by co-adsorbed water, which results in a decrease of the barrier by 0.2 eV.

On the contrary to the key intermediate hydrogenation and dehydrogenation reactions, no enhancement effect was observed for subsequent dehydroxylation and deoxygenation reactions ($\mathbf{TS_6}$ and $\mathbf{TS_7}$ respectively). The new NEB calculations revealed that the dehydroxylation and deoxygenation minimum energy paths follow reaction coordinates in which water first diffuses away from the reactant before the transition state is formed. As the presence of a coadsorbed water did not lower these highest barriers of the pathway, we chose to not investigate the following hydrogenation steps towards alkane formation further.

The reaction energies and barriers for both butanol and butanone formation from the key intermediate are modified due to the co-adsorbed water on both surfaces. However, the barrier for butanone formation (dehydrogenation) from the key intermediate still remains lower than the butanol formation (hydrogenation) barrier on both metal surfaces. As the subsequent reaction steps were found to not be significantly enhanced/hindered by the presence of water, this suggests that co-adsorbed water is not responsible for the promotion of butane production through the butanol pathway.

Additional microkinetic simulations were performed at 553 K for both surfaces in order to verify whether the co-adsorbed water could affect the reaction kinetics. Barriers (forward and backward) for the dehydrogenation and hydrogenation of the key intermediate were changed according to Fig. 5. No further modifications were made to the models.

On Ru(0001), the changes to the reaction barriers result in a slightly increased butanol selectivity at the expense of butanone and butane. The relative decrease in butanone and butane production is ca. 60%. Butanone deoxygenation is still the favoured pathway for butane production. On Rh(111), the butanol selectivity is greatly decreased from over 90% to 30%, while butanone selectivity is increased from < 10 % to ca 70%. Butane selectivity remains low, and the favoured pathway for its formation is now the butanone deoxygenation route, as it contributes over 94% to the formation rate.

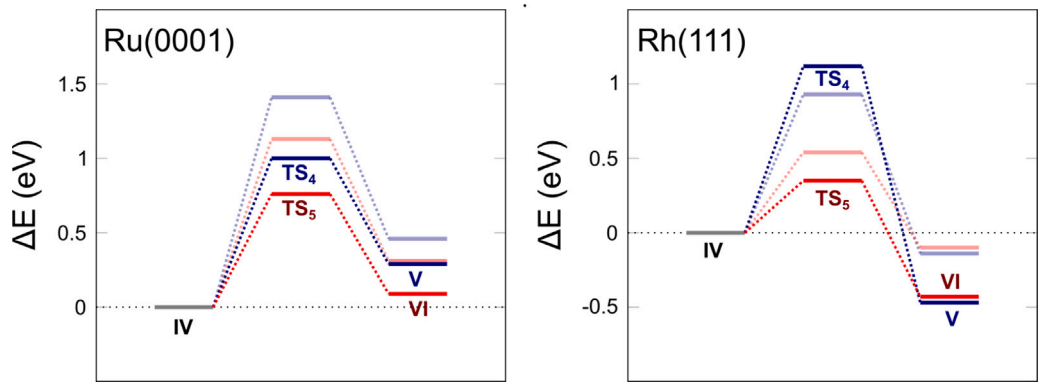

Fig. 7. Modified PES for alcohol and ketone formation for ruthenium (left) and rhodium (right) surface with a co-adsorbed H_2O molecule. The energy of the adsorbed key intermediate **IV** is set to 0. The PES for unmodified unit cells is shown for reference in a paler colour.

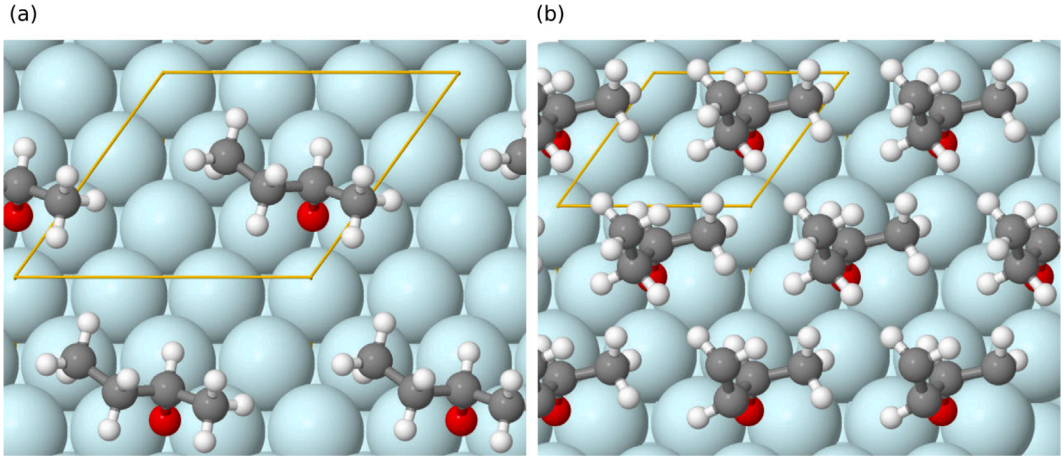

Fig. 8. The optimized structure of the key intermediate **IV** at a coverage of (a) 1/9 ML and (b) 1/4 ML on Ru(0001). The unit cell of the periodic structure is indicated in yellow outlines.

3.3.2. *Effect of higher surface coverage*

In general, increasing surface coverage may substantially modify the reaction selectivity, as shown for e.g. acrolein hydrogenation on Pt and Pd surfaces [40] and cinnamalaniline conversion on Ir [41]. Typically, the surface supercell is chosen to be large enough to accommodate adsorbed species so that lateral interactions between adjacent periodic images are not too large, but keeping the surface small enough so that the computations are not too costly. Using a very large supercell mimics low surface coverage, while using a smaller supercell mimics a higher coverage. At high coverage conditions the steric effects between adsorbates become more prominent. Thus, changing the size of a unit cell effectively modifies the reaction energy profile, which in turn tunes the reaction selectivity.

The possible role of steric effects on the chemoselectivity of GVL conversion were studied by increasing reactant coverage to 1/4 ML on the Ru(0001) surface. Again, the key intermediate was used as a starting point. Fig. 8 displays the favourable adsorption structures for the key intermediate at low and high coverages. While at low coverage the key intermediate binds to a hollow site via oxygen and favours parallel configuration, at 1/4 ML coverage the methyl group tail points away from the surface due to the steric repulsion between the adjacent key intermediate species. Fig. 9 presents the potential energy surface at 1/4 ML coverage starting from the key intermediate.

At 1/4 ML coverage, butanol formation becomes energetically more favourable than at 1/9 ML coverage, whereas the opposite behaviour is seen for butanone formation. The barrier height difference between hydrogenation to butanol $\mathbf{TS_4}$ and dehydrogenation to butanone $\mathbf{TS_5}$ reduces down to 0.02 eV making these steps kinetically competitive. However, the butanol dehydroxylation reaction proceeding via $\mathbf{TS_6}$ remains still highly unfavourable with an activation energy of 1.56 eV. Along the pathway from butanone to butane, the highest barrier is found for the deoxygenation step, $\mathbf{TS_7}$ and it is ~ 0.3 eV higher than at 1/9 ML coverage, making the conversion towards alkane less feasible. The adsorption energies of butanol, butanone, and butane products are −0.37, −0.32, and −0.07 eV, respectively, which are slightly less exothermic than at 1/9 ML, i.e. all products are slightly less stable at the higher coverage.

The high coverage results suggest that the selectivity towards butanol increases with increasing coverage while simultaneously butane production decreases. Microkinetic simulation at 553 K with the modified energetics of the 1/4 ML coverage on Ru(0001) shows that only butanol is produced (the rate is equal to the key intermediate feed rate). This is consistent with the DFT results, as the butanol formation barrier is lowered, while the dehydroxylation barrier stays prohibitively high.

3.4. *MKM discussion*

The MKM simulations suggest that the selectivity towards the products is controlled mainly by the hydrogenation of the key intermediate to the butanol and subsequent desorption from the surface, which is overall kinetically more favourable than butanone or butane production on both metal surfaces. This is due to the facile hydrogenation of the key intermediate that benefits from the high surface coverage, as opposed to the dehydrogenation into butanone that requires empty sites on the surface. Experimentally, butane production is observed on both Ru and Rh catalysts at relatively high GVL conversions. Here, the

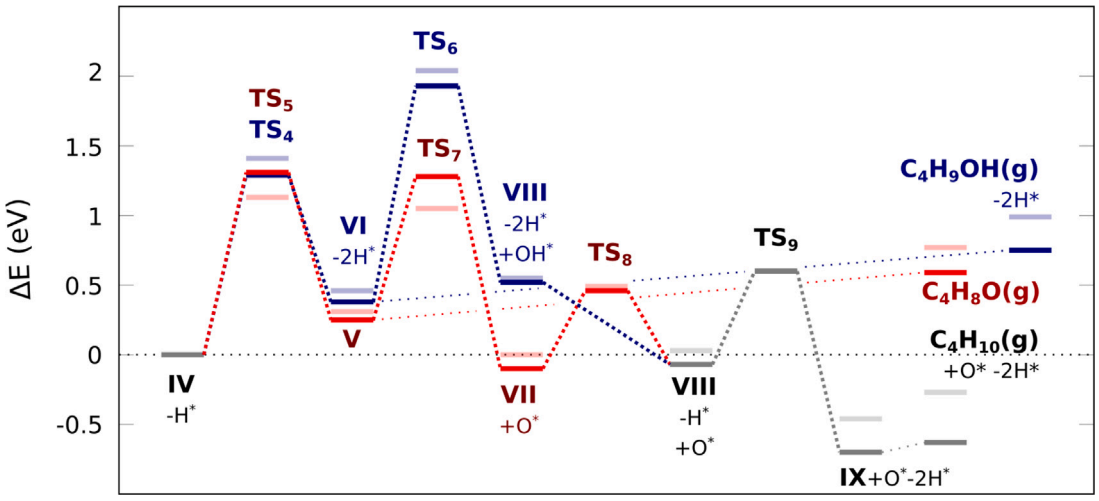

Fig. 9. Modified PES for butane, butanol, and butanone formation on Ru(0001) at 1/4 ML coverage. The energy of the key intermediate **IV** is set to 0 eV. The unmodified PES is shown as reference in a pale colour.

tested conditions more closely correspond to initial zero conversion conditions. However, accurately simulating higher conversions would require much more detailed kinetic descriptions of the diffusion and adsorption processes of the reactant and product molecules within the microkinetic reaction network. This is beyond the scope of this work, but is an interesting future direction. Another possibility is that butanol conversion takes place on a different active site, such as a metal step-edge or on the support oxide [42].

4. Conclusion

The conducted DFT calculations together with the microkinetic modelling provides insight into the selectivity towards ketone, alcohol, and alkane products of hydrodeoxygenative (HDO) treatment of γ-valerolactone over Ru(0001) and Rh(111). The mechanism involves two parallel pathways that lead to alkane production through either an alcohol or ketone surface intermediate, both of which can also desorb from the surface before reacting further. The alcohol and ketone production steps share a common surface intermediate, and are therefore competing reactions. At all conditions tested with microkinetic modelling, alcohol production was found to be most favourable among the three considered HDO products on both surfaces. Ru was also capable of producing significant amounts of alkane through the ketone pathway. While alkane selectivity was extremely low on Rh, the reaction was shown to proceed through both the alcohol and ketone intermediates. The results suggest that both alcohols and ketones could be important reaction intermediates towards alkane production on Ru and Rh.

CRediT authorship contribution statement

Minttu M. Kauppinen: Writing – review & editing, Visualization, Validation, Software, Investigation, Formal analysis, Data curation, Conceptualization. **Ewa N. Słapa:** Writing – original draft, Visualization, Validation, Investigation, Formal analysis, Data curation. **José Luis González Escobedo:** Writing – review & editing, Investigation, Data curation. **Riikka L. Puurunen:** Writing – review & editing, Supervision, Resources, Project administration, Funding acquisition, Conceptualization. **Karoliina Honkala:** Writing – review & editing, Supervision, Resources, Project administration, Funding acquisition, Conceptualization.

Declaration of competing interest

The authors declare the following financial interests/personal relationships which may be considered as potential competing interests: Ewa Slapa reports financial support was provided by Research Council of Finland. Jose Luis Gonzales Escobedo and Riikka Puurunen reports financial support was provided by Neste Corp. Jose Luis Gonzales Escobedo reports financial support was provided by Fortum Foundation. Jose Luiz Gonzales Escobedo reports financial support was provided by Finnish Foundation for Technology Promotion. If there are other authors, they declare that they have no known competing financial interests or personal relationships that could have appeared to influence the work reported in this paper.

Acknowledgments

The computational work was funded by Research Council of Finland (307623) and University of Jyväskylä. The electronic structure calculations were made possible by the computational resources provided by the CSC — IT Center for Science, Espoo, Finland (https://www.csc.fi/en/) and FGCI. The experiments on which this work is based (Supporting Information) were funded by Neste Corporation. J. L. G. E. acknowledges funding from Fortum Foundation, Finland (number 201800142) and from the Finnish Foundation for Technology Promotion, Finland (number 6712).

Appendix A. Supporting information available

See supporting information for the molar yields (%) of main product groups obtained in HDO experiments with γ-nonalactone using Ru/ZrO_2 and Rh/ZrO_2 catalysts, and tabulated vibrational frequencies for surface species, gas phase species, and transition states used in the microkinetic models. The computed structures presented in this study are openly available to download from the Finnish Fairdata service at https://doi.org/10.23729/ea2e013c-52ac-49d3-9c70-106b49e98920.

Data availability

The link to the computational data is given in the manuscript.

References

[1] G. Lopez, D. Keiner, M. Fasihi, T. Koiranen, C. Breyer, From fossil to green chemicals: sustainable pathways and new carbon feedstocks for the global chemical industry, Energ. Environ. Sci. 16 (7) (2023) 2879–2909.

[2] R. Rinaldi, F. Schüth, Acid hydrolysis of cellulose as the entry point into biorefinery schemes, ChemSusChem 2 (12) (2009) 1096–1107.

[3] T. Werpy, G. Petersen, Top Value Added Chemicals from Biomass: Volume I – Results of Screening for Potential Candidates from Sugars and Synthesis Gas, National Renewable Energy Lab., Golden, CO (US), United States, 2004.

[4] R.W. Blessing, L. Petrus, A catalytic process for the dimerization of Levulinic acid and the preparation of diesters from these dimers obtainable by such process, 2006, Patent WO 2006/056591 A1.

[5] M. Käldström, M. Lindblad, K. Lamminpää, S. Wallenius, S. Toppinen, Carbon chain length increase reactions of platform molecules derived from C_5 and C_6 sugars, Ind. Eng. Chem. Res. 56 (45) (2017) 13356–13366.

[6] L. Faba, E. Díaz, S. Ordóñez, Base-catalyzed condensation of Levulinic acid: A new biorefinery upgrading approach, ChemCatChem 8 (8) (2016) 1490–1494.

[7] Z. Li, J. Zhang, M.M. Nielsen, H. Wang, C. Chen, J. Xu, Y. Wang, T. Deng, X. Hou, Efficient C–C bond formation between two Levulinic acid molecules to produce C10 compounds with the cooperation effect of Lewis and Brønsted acids, ACS Sustain. Chem. Eng. 6 (5) (2018) 5708–5711.

[8] A.S. Amarasekara, B. Wiredu, T.L. Grady, R.G. Obregon, D. Margetić, Solid acid catalyzed aldol dimerization of levulinic acid for the preparation of C10 renewable fuel and chemical feedstocks, Catal. Commun. 124 (2019) 6–11.

[9] P.J. Van den Brink, K.L. Von Hebel, J.-P. Lange, L. Petrus, Process for the hydrogenation of a lactone or of a carboxylic acid or an ester having a gamma-carbonyl group, 2006, Patent WO 2006/067171 A1.

[10] E. Mäkelä, J.L. González Escobedo, M. Lindblad, M. Käldström, H. Meriö-Talvio, H. Jiang, R. Puurunen, R. Karinen, Hydrodeoxygenation of Levulinic acid dimers on a zirconia-supported ruthenium catalyst, Catalysts 10 (2) (2020) 200.

[11] J.L. González Escobedo, E. Mäkelä, A. Braunschweiler, J. Lehtonen, M. Lindblad, R.L. Puurunen, R. Karinen, Solvent-free hydrodeoxygenation of γ-nonalactone on noble metal catalysts supported on zirconia, Top Catal. 62 (7–11) (2019) 724–737.

[12] K. Yan, Y. Yang, J. Chai, Y. Lu, Catalytic reactions of gamma-valerolactone: A platform to fuels and value-added chemicals, Appl. Catal. B: Environ. 179 (2015) 292–304.

[13] J.J. Bozell, L. Moens, D. Elliott, Y. Wang, G. Neuenscwander, S. Fitzpatrick, R. Bilski, J. Jarnefeld, Production of levulinic acid and use as a platform chemical for derived products, Renew. Sust. Energ. Rev. 28 (3) (2000) 227–239.

[14] M.G. Al-Shaal, A. Dzierbinski, R. Palkovits, Solvent-free γ-valerolactone hydrogenation to 2-methyltetrahydrofuran catalysed by Ru/C: a reaction network analysis, Green Chem. 16 (2014) 1358–1364.

[15] J.Q. Bond, D. Wang, D.M. Alonso, J.A. Dumesic, Interconversion between γ-valerolactone and pentenoic acid combined with decarboxylation to form butene over silica/alumina, J. Catal. 281 (2) (2011) 290–299.

[16] J.C. Serrano-Ruiz, D.J. Braden, R.M. West, J.A. Dumesic, Conversion of cellulose to hydrocarbon fuels by progressive removal of oxygen, Appl. Catal. B 100 (1) (2010) 184–189.

[17] A. Rozenblit, A.J. Avoian, Q. Tan, T. Sooknoi, D.E. Resasco, Reaction mechanism of aqueous-phase conversion of γ-valerolactone (GVL) over a Ru/C catalyst, J. Energy Chem. 25 (6) (2016) 1008–1014.

[18] R.M. Bababrik, B. Wang, D.E. Resasco, Reaction mechanism for the conversion of γ-valerolactone (GVL) over a ru catalyst: A first-principles study, Ind. Eng. Chem. Res. (12) (2017) 3217–3222.

[19] J. Enkovaara, C. Rostgaard, J.J. Mortensen, J. Chen, M. Dulak, L. Ferrighi, J. Gavnholt, C. Glinsvad, V. Haikola, H.A. Hansen, H.H. Kristoffersen, M. Kuisma, A.H. Larsen, L. Lehtovaara, M. Ljungberg, O. Lopez-Acevedo, P.G. Moses, J. Ojanen, T. Olsen, V. Petzold, N.A. Romero, J. Stausholm-Møller, M. Strange, G.A. Tritsaris, M. Vanin, M. Walter, B. Hammer, H. Häkkinen, G.K.H. Madsen, R.M. Nieminen, J.K. Nørskov, M. Puska, T.T. Rantala, J. Schiøtz, K.S. Thygesen, K. Jacobsen, Electronic structure calculations with GPAW: a real-space implementation of the projector augmented-wave method, J. Phys.: Condens. Matter. 22 (25) (2010) 253202.

[20] J.J. Mortensen, L.B. Hansen, K.W. Jacobsen, Real-space grid implementation of the projector augmented wave method, Phys. Rev. B 71 (2005) 035109.

[21] A.H. Larsen, J.J. rgen Mortensen, J. Blomqvist, I.E. Castelli, R. Christensen, M.D. ak, J. Friis, M.N. Groves, B. rk Hammer, C. Hargus, E.D. Hermes, P.C. Jennings, P.B. Jensen, J. Kermode, J.R. Kitchin, E.L. Kolsbjerg, J. Kubal, K. Kaasbjerg, S. Lysgaard, J.B. Maronsson, T. Maxson, T. Olsen, L. Pastewka, A. Peterson, C. Rostgaard, J.S. tz, O. Schütt, M. Strange, K.S. Thygesen, T. Vegge, L. Vilhelmsen, M. Walter, Z. Zeng, K.W. Jacobsen, The atomic simulation environment—a python library for working with atoms, J. Phys.: Condens. Matter. 29 (27) (2017) 273002.

[22] S.R. Bahn, K.W. Jacobsen, An object-oriented scripting interface to a legacy electronic structure code, Comput. Sci. Eng. 4 (3) (2002) 56–66.

[23] J. Wellendorff, K.T. Lundgaard, A. Møgelhøj, V. Petzold, D.D. Landis, J.K. Nø rskov, T. Bligaard, K.W. Jacobsen, Density functionals for surface science: Exchange-correlation model development with Bayesian error estimation, Phys. Rev. B 85 (2012) 235149.

[24] P.E. Blöchl, Projector augmented-wave method, Phys. Rev. B 50 (1994) 17953–17979.

[25] E.L. Kolsbjerg, M.N. Groves, B. rk Hammer, An automated nudged elastic band method, J. Chem. Phys. 145 (9) (2016) 094107.

[26] G. Henkelman, B.P. Uberuaga, H. Jónsson, A climbing image nudged elastic band method for finding saddle points and minimum energy paths, J. Chem. Phys. 113 (22) (2000) 9901–9904.

[27] H. Jónsson, G. Mills, K. Jacobsen, in: B.J. Berne, G. Ciccotti, D.F. Coker (Eds.), Classical and Quantum Dynamics in Condensed Phase Simulations, World Scientific, 1998.

[28] G. Henkelman, H. Jónsson, Improved tangent estimate in the nudged elastic band method for finding minimum energy paths and saddle points, J. Chem. Phys. 113 (22) (2000) 9978–9985.

[29] P. Virtanen, R. Gommers, T.E. Oliphant, M. Haberland, T. Reddy, D. Cournapeau, E. Burovski, P. Peterson, W. Weckesser, J. Bright, S.J. van der Walt, M. Brett, J. Wilson, K.J. Millman, N. Mayorov, A.R.J. Nelson, E. Jones, R. Kern, E. Larson, C. Carey, İ. Polat, Y. Feng, E.W. Moore, J. VanderPlas, D. Laxalde, J. Perktold, R. Cimrman, I. Henriksen, E.A. Quintero, C.R. Harris, A.M. Archibald, A.H. Ribeiro, F. Pedregosa, P. van Mulbregt, SciPy 1.0 Contributors, SciPy 1.0: Fundamental Algorithms for Scientific Computing in Python, Nat. Methods 17 (2020) 261–272.

[30] O. Mamun, E. Walker, M. Faheem, J.Q. Bond, A. Heyden, Theoretical investigation of the hydrodeoxygenation of Levulinic acid to γ-valerolactone over Ru(0001), ACS Catal. 7 (1) (2017) 215–228.

[31] C. Michel, J. Zaffran, A.M. Ruppert, J. Matras-Michalska, M. Jędrzejczyk, J. Grams, P. Sautet, Role of water in metal catalyst performance for ketone hydrogenation: a joint experimental and theoretical study on levulinic acid conversion into gamma-valerolactone, Chem. Commun. 50 (2014) 12450–12453.

[32] R.A. Dagle, Y. Wang, G.-G. Xia, J.J. Strohm, J. Holladay, D.R. Palo, Selective CO methanation catalysts for fuel processing applications, Appl. Catal. A Gen. 326 (2) (2007) 213–218.

[33] B. Miao, S.S.K. Ma, X. Wang, H. Su, S.H. Chan, Catalysis mechanisms of CO2 and CO methanation, Catal. Sci. Technol. 6 (2016) 4048–4058.

[34] L. Foppa, M. Iannuzzi, C. Copéret, A. Comas-Vives, CO methanation on ruthenium flat and stepped surfaces: Key role of H-transfers and entropy revealed by ab initio molecular dynamics, J. Catal 371 (2019) 270–275.

[35] M. Abdelgaid, E.V. Miu, H. Kwon, M.M. Kauppinen, H. Grönbeck, G. Mpourmpakis, Multiscale modeling reveals aluminum nitride as an efficient propane dehydrogenation catalyst, Catal. Sci. Technol. 13 (2023) 3527–3536.

[36] M.M. Kauppinen, N. Daelman, N. López, K. Honkala, The role of polaronic states in the enhancement of CO oxidation by single-atom Pt/CeO2, J. Catal 423 (2023) 26–33.

[37] M. Kauppinen, A. Posada-Borbón, H. Grönbeck, Methanol synthesis over PdIn, In2O3, and CuZn from first-principles microkinetics: Similarities and differences, J. Phys. Chem. C 126 (36) (2022) 15235–15246.

[38] M.M. Kauppinen, M.M. Melander, A.S. Bazhenov, K. Honkala, Unraveling the role of the Rh–ZrO2 interface in the water–gas-shift reaction via a first-principles microkinetic study, ACS Catal. 8 (12) (2018) 11633–11647.

[39] S. Hong, M.M. Kauppinen, E.V. Miu, G. Mpourmpakis, H. Grönbeck, First-principles microkinetic modeling of partial methane oxidation over graphene-stabilized single-atom Fe-catalysts, Catal. Sci. Technol. 13 (2023) 6999–7010.

[40] S. Tuokko, P.M. Pihko, K. Honkala, First principles calculations for hydrogenation of acrolein on Pd and Pt: Chemoselectivity depends on steric effects on the surface, Angew. Chem. Int. Edn 55 (5) (2016) 1670–1674.

[41] R. Savela, N.D. Shcherban, M.M. Melander, I. Bezverkhyy, I.L. Simakova, O. Långvik, E. Kholkina, T. Schindler, A. Krauß, K. Honkala, D.Y. Murzin, R. Leino, Chemoselective heterogeneous iridium catalyzed hydrogenation of cinnamalaniline, Catal. Sci. Technol. 11 (2021) 1481–1496.

[42] W. Xia, F. Wang, X. Mu, K. Chen, Remarkably enhanced selectivity for conversion of ethanol to propylene over ZrO2 catalysts, Fuel Process. Technol. 166 (2017) 140–145.